ELSEVIER

Effects of rotating gaseous flows on transient droplet dynamics and heating

Jun Xin * **and Constantine M. Megaridis**
Department of Mechanical Engineering, The University of Illinois at Chicago, Chicago, IL, USA

In this paper, the effects of rotating gaseous flows on transient droplet dynamics and heating are investigated theoretically. The idealized flow configuration considered involves a periodic linear array of nonvaporizing droplets trapped on the axis of a rotating, infinitely long, gaseous cylinder, which drives the droplet spin-up. The effects of the induced secondary motion and rotational Reynolds number on heat transfer in both phases are examined. The results show that initially quiescent droplets can be rotationally accelerated within relatively short time periods compared with their evaporation lifetimes and that the characteristic times for transient heating and spin-up are of comparable magnitude. In addition, the effects of rotation on droplet heating are found to be insignificant for small droplets (of the order of 100 μm or smaller) and the corresponding low values of rotational Reynolds numbers.

Keywords: droplet array; rotation; spinning; transient dynamics and heating

Introduction

Spray combustion is an important energy conversion method in many practical combustion systems, such as gas turbines, diesel engines, or liquid-fired furnaces. The evaporation rate of individual droplets is frequently a critical factor in improving combustion efficiency and reducing exhaust emissions. To this end, understanding of the heating and evaporation characteristics of individual droplets is pertinent to combustion technologies incorporating dispersed liquid fuels.

Since the single-droplet evaporation and combustion model based on the assumption of spherical symmetry was established (Godsave 1953; Spalding 1953), a number of research activities have concentrated on this area (Law 1982; Faeth 1983). However, in most practical spray applications, droplets are injected with relative velocity with respect to the ambient medium, therefore, the spherical symmetry assumption is no longer valid. Furthermore, relative motion between dispersed liquids and ambient gases results in the development of shear stresses along the gas/liquid interface that induce internal droplet circulation. Standard axisymmetric configurations, where a droplet is suddenly exposed to a hot uniform velocity stream, have been considered to examine the interactions between gas and liquid, as well as the effects of Hill's toroidal circulation (Hill 1894) on droplet heatup and evaporation. Recent comprehensive reviews of studies in this area are given by Sirignano (1983, 1993) and Dwyer (1989).

In most spray combustion applications, strong vortices are induced to enhance mixing and improve efficiency. As a result, the assumption of uniform flow around a droplet is justified only when droplet sizes are appreciably smaller than the characteristic length scale of the surrounding flow structures. Because in most practical fuel sprays typical droplet sizes are of the order of 100 μm, structures larger than a few centimeters may be consistent with the assumption of uniform ambient flow; whereas, fine (submillimeter) turbulent structures are incompatible with this assumption. Considering that most practical flows are turbulent and feature high levels of fluctuating vorticity (Tennekes and Lumley 1972), it is important to evaluate the role of flow rotation in droplet gasification. However, as of today, little work has been done on the interaction of dispersed liquids and rotating flows.

The shape and stability of rotating droplets has been the subject of studies for more than a century. Fundamental studies in this field date back to Plateau's work in 1863 (Plateau 1863). The interpretation of phenomena related to nuclear fission has revived interest in the classical problem of equilibrium and stability of a rotating liquid mass held together by surface tension. The parameter used as a criterion for droplet sphericity under rigid-body rotating conditions is defined by

$$\Sigma = \Delta\rho\Omega^2 r_0^3/8\sigma \tag{1}$$

where Ω denotes the angular velocity of rotation, r_0 the radius of the drop, $\Delta\rho$ the density difference between the liquid and the surrounding fluid, and σ the surface tension coefficient. Theoretical and experimental studies (Chandrasekhar 1965; Brown and Scriven 1980; Wang et al. 1986) have shown that the shape deformation is slight for low values of Σ (< 0.45). From Equation 1, it is clear that the larger the droplet size, the lower the maximum allowable angular velocity before deformation needs to be considered.

The influence of droplet rotation on evaporation/combustion characteristics was recently examined by Pearlman and Sohrab

Address reprint requests to Prof. C. M. Megaridis, Dept. of Mechanical Eng. (M/C 251), Univ. Illinois at Chicago, 842 W. Taylor St., Chicago IL 60607-7022.
* Currently at Dept. of Mechanical Engineering, University of Wisconsin, Madison WI 53706.

Received 27 January 1995; accepted 14 September 1995

655 Avenue of the Americas, New York, NY 10010

0142-727X/96/$15.00
SSDI 0142-727X(95)00081-X

(1991, 1993), who used a fiber-supported spinning droplet of heptane and a rotating porous sphere fed with butane gas. It was reported that rotation enhances the rate of liquid evaporation, and thus results in substantially shorter droplet lifetimes. However, because of experimental limitations, the measurements of Pearlman and Sohrab involved mm-sized fiber-suspended droplets, and cm-sized porous spheres, thus making their results not directly applicable to substantially smaller droplets, which are more appropriate to spray combustion. It is also noted that Pearlman and Sohrab did not address the detailed heat transfer dynamics between liquid and gas phases. Lozinski and Matalon (1992) employed an analytical approach to examine droplet spinning effects on steady-state liquid evaporation under low values of the rotational Reynolds number. They considered zero relative translational velocity between the droplet and the ambient gas (i.e., axisymmetry) and assumed the liquid-fuel temperature to be uniform and constant. It was reported that the effect of droplet spinning on evaporation rates was very weak under the conditions investigated therein (Lozinski and Matalon). Hou and Lin (1993) examined the influence of flow rotation on droplet combustion and evaporation using a burning liquid-pool experimental system and a numerical model considering a nonreactive, rotating stagnation point flow. They showed that both convection and diffusion transports are weakened by flow rotation, resulting in the suppression of the evaporation strength of the liquid. The liquid-pool configuration of Hou and Lin was intended to simulate the gasification process near the forward stagnation region of the droplet, but may not provide a good description away from that region (in the wake, for example). In another recent study, Megaridis et al. (1994) examined the internal dynamics of a suspended mm-sized droplet that was induced to rotate by exposure to a gaseous cross stream. The combined theoretical/experimental study focused on fluid dynamical aspects at low values of rotational Reynolds number and showed that helical droplet internal flows develop not only temporarily during the transient phases of droplet rotation, but may also develop at steady state as a result of kinematic nonuniformities on the droplet surface. The interactions between gas and liquid phases, as well as evaporation were not modeled in that study.

When a fuel droplet acquires angular velocity — either during atomization, or by encountering nonuniform ambient flows (Kim et al. 1993) — it is expected that the angular velocity vector would undergo random fluctuations in magnitude as well as orientation (Pearlman and Sohrab 1991). A complete model would obviously require a three-dimensional approach that is out of the scope of the current work. In this paper, the practical gas/droplet interactions within turbulent eddies are simplified by considering a steadily rotating or impulsively started, infinitely long, gaseous cylindrical container (simulating a tubular vortex) with a periodic droplet array trapped along its axis (Figure 1A). The unsteady fluid dynamics and heat transfer of both phases are addressed in the following, in order to define the role, if any, rotation may play in heating and evaporation characteristics for droplets of O(100 μm) radius. The dimensions of interest for the problem considered are defined in Figure 1.

Physical model and governing equations

Physical model description

The physical model studied herein is shown in Figure 1, where rotation around the X-axis is considered to be the primary motion. The infinitely long cylinder (Figure 1A) contains a viscous, incompressible gaseous medium. A periodic array of droplets remains trapped along the axis of the cylinder, and the distance between two adjacent droplets is $2H$. The droplet array remains coincident with the axis of the cylinder, and the droplet interspacing ($2H$) is assumed to be constant. Rotating conditions are imposed on the outer surface of the gaseous cylinder, thus inducing the inner gas and eventually the droplets to rotate. Because the imposed rotation boundary conditions are generally time dependent, the problem in hand is transient and axisymmetric with respect to the X-axis. Two symmetry planes are noted in

Notation

c_p specific heat
f rotation frequency
H half droplet spacing
k thermal conductivity
M dimensionless torque
p_g dimensionless gas pressure, normalized with respect to $\rho_g(\Omega_{\min}R_0)^2$
p_l dimensionless liquid pressure, normalized with respect to $\rho_l(\Omega_{\min}R_0)^2$
P_g dimensional gas pressure
P_l dimensional liquid pressure
r dimensionless radial coordinate, normalized with respect to r_0
r_0 droplet radius
R_0 radius of cylindrical rotating tube
Re_g rotational gas Reynolds number, $\rho_g\Omega_{\min}R_0r_0/\mu_g$
Re_l rotational liquid Reynolds number, $\rho_l\Omega_{\min}R_0r_0/\mu_l$
T temperature
v velocity; normalized with respect to $\Omega_{\min}R_0$
x, y dimensionless axial and radial coordinates, normalized with respect to r_0
X, Y dimensional axial and radial cylindrical coordinates

Greek

α thermal diffusivity
η computational domain coordinate
θ polar coordinate (collatitude)
μ dynamic viscosity
ξ computational domain coordinate
ρ density
σ surface tension coefficient
Σ rotating droplet deformation parameter, Equation 1
τ nondimensional time, normalized with respect to $r_0/\Omega_{\min}R_0$, also stress
φ azimuthal coordinate
Ω angular velocity

Subscripts

g gas
l liquid
min minimum
r radial
s droplet interface
x horizontal
y vertical
θ polar
φ azimuthal

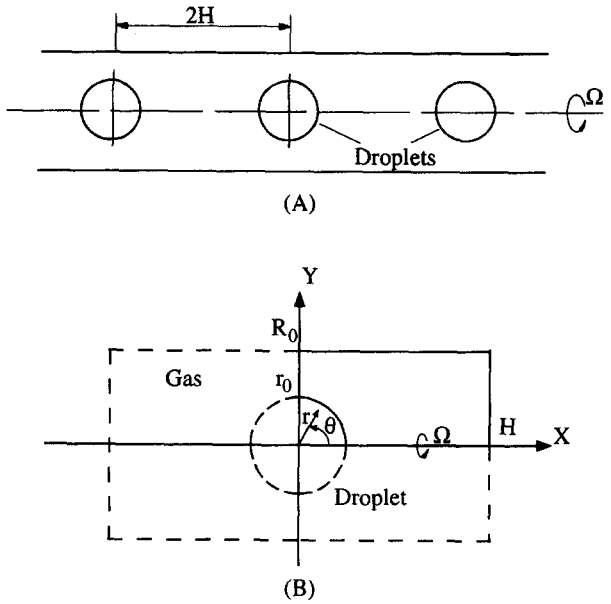

Figure 1 Schematic of rotational flow configuration; (A) linear array of droplets in rotating gaseous tube, (B) computational domain

Figure 1B: $X = 0$, and $X = H$. Because of these symmetries, the physical domain analyzed is restricted only to the upper right quadrant of Figure 1B (bound by the solid lines).

The droplet rotating conditions considered in this study are consistent with the assumption of droplet sphericity (negligible deformation). In fact, most cases involving liquid-hydrocarbon droplets and ambient conditions characteristic of a spray combustor satisfy the condition $\Sigma < 0.45$, therefore, droplet deformation attributable to spinning can be safely neglected. For example, a 200 μm-diameter n-decane droplet rotating in a 1000 K air environment needs to reach a rotation frequency above 1500 Hz for shape deformation to become important. Such high frequencies are highly unprobable in practical systems, therefore, the assumption of spherical shape for the spinning droplets considered herein is fully justified. Finally, the thermophysical properties of both gas and liquid phases are assumed to be constant.

Although a complete treatment of the relevant fluid dynamical and heat transport mechanisms is considered in this investigation, liquid evaporation has not been modeled. In that respect, the results of this work are relevant to nonvolatile liquids (heavy fuels, for example). However, the examined effect of rotation on heat transport rates may also provide useful insight to guide subsequent investigations involving evaporating fuels.

Two physical coordinate systems are used in formulation (see Figure 1B); spherical coordinates for the droplet interior (r, θ, φ), and cylindrical coordinates for the gaseous volume (X, Y, φ). The origins of the two physical coordinate systems coincide with the droplet center. In addition, a nonorthogonal generalized coordinate system (ξ, η) is used to facilitate the gas-phase computation. In the following, the governing equations are given for both phases, along with the corresponding boundary and initial conditions.

Formulation

The continuity, momentum, and energy equations inside and outside the droplet, as well as the relevant boundary conditions are nondimensionalized using the droplet radius r_0 as the characteristic length and the azimuthal velocity ΩR_0 as the characteristic velocity. Because the imposed angular velocity Ω on the sidewall $(Y = R_0)$ is in general variable with X, its minimum value $\Omega_{\min}$ is used for the calculation of the characteristic velocity. The characteristic time is defined by the ratio $r_0/\Omega_{\min} R_0$. The pressures P_g (gas) and P_l (liquid) are nondimensionalized with respect to $\rho_g(\Omega_{\min} R_0)^2$, and $\rho_l(\Omega_{\min} R_0)^2$, respectively. The dimensionless form of the governing equations is given below.

- *Gas phase (cylindrical coordinates)*:

Continuity:

$$\frac{1}{y}\frac{\partial}{\partial y}(y v_{y,g}) + \frac{\partial v_{x,g}}{\partial x} = 0 \tag{2}$$

x-momentum:

$$\frac{\partial v_{x,g}}{\partial \tau} + v_{y,g}\frac{\partial v_{x,g}}{\partial y} + v_{x,g}\frac{\partial v_{x,g}}{\partial x} = -\frac{\partial p_g}{\partial x} + \frac{1}{\mathrm{Re}_g}\left[\frac{1}{y}\frac{\partial}{\partial y}\left(y\frac{\partial v_{x,g}}{\partial y}\right) + \frac{\partial^2 v_{x,g}}{\partial x^2}\right] \tag{3}$$

y-momentum:

$$\frac{\partial v_{y,g}}{\partial \tau} + v_{y,g}\frac{\partial v_{y,g}}{\partial y} + v_{x,g}\frac{\partial v_{y,g}}{\partial x} - \frac{v_{\varphi,g}^2}{y} = -\frac{\partial p_g}{\partial y} + \frac{1}{\mathrm{Re}_g}\left[\frac{1}{y}\frac{\partial}{\partial y}\left(y\frac{\partial v_{y,g}}{\partial y}\right) + \frac{\partial^2 v_{y,g}}{\partial x^2} - \frac{v_{y,g}}{y^2}\right] \tag{4}$$

φ-momentum:

$$\frac{\partial v_{\varphi,g}}{\partial \tau} + v_{y,g}\frac{\partial v_{\varphi,g}}{\partial y} + v_{x,g}\frac{\partial v_{\varphi,g}}{\partial x} + \frac{v_{y,g} v_{\varphi,g}}{y} = \frac{1}{\mathrm{Re}_g}\left[\frac{1}{y}\frac{\partial}{\partial y}\left(y\frac{\partial v_{\varphi,g}}{\partial y}\right) + \frac{\partial^2 v_{\varphi,g}}{\partial x^2} - \frac{v_{\varphi,g}}{y^2}\right] \tag{5}$$

Energy:

$$\frac{\partial T_g}{\partial \tau} + v_{y,g}\frac{\partial T_g}{\partial y} + v_{x,g}\frac{\partial T_g}{\partial x} = \frac{\alpha_g}{R_0 r_0 \Omega_{\min}}\left[\frac{1}{y}\frac{\partial}{\partial y}\left(y\frac{\partial T_g}{\partial y}\right) + \frac{\partial^2 T_g}{\partial x^2}\right] \tag{6}$$

In the above, $v_{x,g}$, $v_{y,g}$, $v_{\varphi,g}$ are the three components of the velocity vector, p_g the pressure, and T_g the temperature. The Reynolds number is

$$\mathrm{Re}_g = \frac{\rho_g \Omega_{\min} R_0 r_0}{\mu_g} \tag{7}$$

and the thermal diffusivity

$$\alpha_g = \frac{k_g}{\rho_g c_{p,g}} \tag{8}$$

- *Liquid Phase (spherical coordinates)*:

Continuity:

$$\frac{1}{r^2}\frac{\partial}{\partial r}(r^2 v_{r,l}) + \frac{1}{r\sin\theta}\frac{\partial}{\partial \theta}(v_{\theta,l}\sin\theta) = 0 \tag{9}$$

r-momentum:

$$\frac{\partial v_{r,l}}{\partial \tau} + v_{r,l}\frac{\partial v_{r,l}}{\partial r} + \frac{v_{\theta,l}}{r}\frac{\partial v_{r,l}}{\partial \theta} - \frac{\left(v_{\theta,l}^2 + v_{\varphi,l}^2\right)}{r} = -\frac{\partial p_l}{\partial r} + \frac{1}{\mathrm{Re}_l}\frac{1}{r^2}\left[\frac{\partial}{\partial r}\left(r^2\frac{\partial v_{r,l}}{\partial r}\right) + \frac{1}{\sin\theta}\frac{\partial}{\partial \theta}\left(\sin\theta\frac{\partial v_{r,l}}{\partial \theta}\right) - 2v_{r,l} - 2\frac{\partial v_{\theta,l}}{\partial \theta} - 2v_{\theta,l}\cot\theta\right] \tag{10}$$

θ-*momentum*:

$$\frac{\partial v_{\theta,l}}{\partial \tau} + v_{r,l}\frac{\partial v_{\theta,l}}{\partial r} + \frac{v_{\theta,l}}{r}\frac{\partial v_{\theta,l}}{\partial \theta} + \frac{\left(v_{r,l}v_{\theta,l} - v_{\varphi,l}^2 \cot\theta\right)}{r}$$
$$= -\frac{1}{r}\frac{\partial p_l}{\partial \theta} + \frac{1}{\mathrm{Re}_l}\frac{1}{r^2}\left[\frac{\partial}{\partial r}\left(r^2\frac{\partial v_{\theta,l}}{\partial r}\right)\right.$$
$$\left. + \frac{1}{\sin\theta}\frac{\partial}{\partial \theta}\left(\sin\theta\frac{\partial v_{\theta,l}}{\partial \theta}\right) + 2\frac{\partial v_{r,l}}{\partial \theta} - \frac{v_{\theta,l}}{\sin^2\theta}\right] \quad (11)$$

φ-*momentum*:

$$\frac{\partial v_{\varphi,l}}{\partial \tau} + v_{r,l}\frac{\partial v_{\varphi,l}}{\partial r} + \frac{v_{\theta,l}}{r}\frac{\partial v_{\varphi,l}}{\partial \theta} + \frac{\left(v_{r,l}v_{\varphi,l} + v_{\theta,l}v_{\varphi,l}\cot\theta\right)}{r}$$
$$= \frac{1}{\mathrm{Re}}\frac{1}{r^2}\left[\frac{\partial}{\partial r}\left(r^2\frac{\partial v_{\varphi,l}}{\partial r}\right) + \frac{1}{\sin\theta}\frac{\partial}{\partial \theta}\left(\sin\theta\frac{\partial v_{\varphi,l}}{\partial \theta}\right) - \frac{v_{\varphi,l}}{\sin^2\theta}\right] \quad (12)$$

Energy:

$$\frac{\partial T_l}{\partial \tau} + v_{r,l}\frac{\partial T_l}{\partial r} + \frac{v_{\theta,l}}{r}\frac{\partial T_l}{\partial \theta}$$
$$= \frac{\alpha_l}{R_0 r_0 \Omega_{\min}}\frac{1}{r^2}\left[\frac{\partial}{\partial r}\left(r^2\frac{\partial T_l}{\partial r}\right) + \frac{1}{\sin\theta}\frac{\partial}{\partial \theta}\left(\sin\theta\frac{\partial T_l}{\partial \theta}\right)\right] \quad (13)$$

where $v_{r,l}$, $v_{\theta,l}$, $v_{\varphi,l}$ are the three components of the velocity vector, p_l the pressure, and T_l the temperature. The Reynolds number is

$$\mathrm{Re}_l = \frac{\rho_l \Omega_{\min} R_0 r_0}{\mu_l} \quad (14)$$

and the thermal diffusivity

$$\alpha_l = \frac{k_l}{\rho_l c_{p,l}} \quad (15)$$

Boundary conditions

The conditions at the gas/droplet interface include continuity of azimuthal and polar shear stress, azimuthal and polar velocity, heat flux and temperature. No fluid is allowed to cross the liquid surface (nonevaporating droplets), therefore, the normal velocities above and below the interface are zero. Because the interface is always spherical, it is more convenient to cast the surface conditions (subscript s) in terms of spherical coordinates (r, θ, φ):

$$\mu_l\left[\frac{\partial v_\theta}{\partial r} - \frac{v_\theta}{r}\right]_{l,s} = \mu_g\left[\frac{\partial v_\theta}{\partial r} - \frac{v_\theta}{r}\right]_{g,s} \quad (16)$$

$$\mu_l\left[\frac{\partial v_\varphi}{\partial r} - \frac{v_\varphi}{r}\right]_{l,s} = \mu_g\left[\frac{\partial v_\varphi}{\partial r} - \frac{v_\varphi}{r}\right]_{g,s} \quad (17)$$

$$v_{\theta,l,s} = v_{\theta,g,s} \quad (18)$$

$$v_{\varphi,l,s} = v_{\varphi,g,s} \quad (19)$$

$$k_l\left(\frac{\partial T}{\partial r}\right)_{l,s} = k_g\left(\frac{\partial T}{\partial r}\right)_{g,s} \quad (20)$$

$$T_{l,s} = T_{g,s} \quad (21)$$

The pressure on both sides of the droplet interface is calculated from the corresponding momentum equation in the radial direction using the most recent values of the velocity field.

The liquid flow boundary conditions are written in spherical coordinates

$$\frac{\partial p_l}{\partial \theta} = \frac{\partial v_{r,l}}{\partial \theta} = \frac{\partial T_l}{\partial \theta} = v_{\theta,l} = v_{\varphi,l} = 0 \; ; \quad \text{at} \quad \theta = 0,\ 0 < r < 1 \quad (22)$$

$$\frac{\partial p_l}{\partial \theta} = \frac{\partial v_{r,l}}{\partial \theta} = \frac{\partial T_l}{\partial \theta} = v_{\theta,l} = \frac{\partial v_{\varphi,l}}{\partial \theta} = 0 \; ; \quad \text{at} \quad \theta = \frac{\pi}{2},\ 0 < r < 1 \quad (23)$$

The gas flow boundary conditions are written in cylindrical coordinates

$$\frac{\partial p_g}{\partial x} = \frac{\partial v_{y,g}}{\partial x} = \frac{\partial v_{\varphi,g}}{\partial x} = \frac{\partial T_g}{\partial x} = v_{x,g} = 0 \; ;$$
$$\text{at} \quad x = 0 \quad \text{or} \quad x = \frac{H}{r_0} \quad (24)$$

$$\frac{\partial p_g}{\partial y} = \frac{\partial v_{x,g}}{\partial y} = \frac{\partial T_g}{\partial y} = v_{y,g} = v_{\varphi,g} = 0 \; ; \quad \text{at} \quad y = 0 \quad (25)$$

$$v_{x,g} = v_{y,g} = 0,\ v_{\varphi,g} = \frac{\Omega(x,t)}{\Omega_{\min}},\ T_g = 1000\ K \; ;$$
$$\text{at} \quad y = \frac{R_0}{r_0} \quad (26)$$

In the above, $\Omega(x, t)$ denotes the imposed rotation at $y = R_0/r_0$, which may be spatially and temporally varying. The pressure boundary condition at the outer cylindrical surface was obtained from the gas-phase momentum equation in the radial direction using the most recent values of the velocity field. It should be mentioned that the pressure boundary conditions listed above are consistent with the velocity boundary conditions and the respective momentum equations.

Computational methodology and algorithm

As seen in Figure 1, the physical domain of the gas flow is not rectangular. To handle this shape, the partial differential equation method (Thompson 1980) was used to generate the numerical grids. The gaseous domain was transformed into a rectangular computational domain with uniform mesh sizes ($\Delta\xi = \Delta\eta = 1$). The original gas-phase governing equations and boundary conditions were transformed with respect to the generalized coordinates (ξ, η). The transformed equations are quite extensive and are not listed here for brevity. By means of this transformation, a problem having simple equations but complex boundary conditions has been transformed to a problem described by complex equations but simpler boundary conditions. A brief description of the computational methodologies is given below for the solution of the Navier–Stokes equations applicable for the laminar, rotating flows considered herein.

The solution of the system of transformed equations was performed numerically using finite-difference discretization techniques. A staggered spatial mesh was utilized, with central difference discretization for the diffusion terms, and upwind differentiation for the convection terms. The time-splitting algorithm was employed for temporal discretization (Dukowicz 1980). At first, the intermediate velocities (except for the azimuthal component) were calculated from the respective momentum equations. Subsequently, the pressure was updated from the modified continuity equation using the successive over-relaxation (SOR) method. The velocities were then corrected using the updated pressure. Finally, the azimuthal velocity and temperature were updated from the azimuthal momentum and energy equa-

tions, respectively. The above steps describe one complete computational cycle, which is repeated for each time step.

The sensitivity of the model predictions to both time-step and numerical grid were examined. Two sets of grids were used to examine grid dependence. In one simulation, grids of 60 (along x) $\times$ 40 (along y) nodes for the gas phase, and 20 (along r) $\times$ 30 (along θ) nodes for the liquid phase were employed. In another simulation, 48 $\times$ 28 nodes for the gas phase and 16 $\times$ 24 nodes for the liquid phase were used. For these two grids, the temperature and velocity values at selected locations of the flow field remained within 2%. Therefore, in all production runs, the 48 $\times$ 28 grid for the gas phase and 16 $\times$ 24 grid for the liquid phase were used along with a nondimensional time step of 10^{-4}, which proved adequate for time-step independent results. The computations were performed on a Cray C90 computer, and each time step required approximately 0.006 CPU seconds.

Results

Model validation

Because no theoretical or experimental data are available for the gas–liquid flow considered herein (Figure 1), comparisons were conducted with the predictions of Briley and Walls (1970) on a similar configuration, which, however, involved gas only. A cylindrical container of height $2H = 0.01$ m, and radius $R_0 = 0.01$ m filled with air at room temperature was considered (Briley and Walls). The initial fluid and container motion was a rigid-body rotation around the cylinder axis with a frequency $f = 1.77$ Hz (corresponding angular velocity $\Omega = 2\pi f = 11.12\ s^{-1}$). The Reynolds number corresponding to these conditions was $Re_g = 66$. At time zero, the container suddenly ceased to rotate. The transient evolution of the induced motion attributable to the sudden deceleration of the container walls was simulated with the current model and the results were compared to those of Briley and Walls. The comparisons were conducted using a dimensionless formulation: lengths were normalized with respect to R_0, velocities with respect to ΩR_0, and times with respect to $1/\Omega$. Figure 2 shows representative isocontours of the azimuthal velocity component (2A) and projected particle pathlines (2B) on the X–Y plane, as produced by the model and corresponding to time $\tau = t\Omega = 0.66$. Note that the pathlines of Figure 2B correspond to instantaneous velocities and that only a quarter of the gaseous flow domain is displayed in that figure due to the associated symmetries. The azimuthal velocity contours shown in Figure 2A depict the severe deceleration of the gas near the container walls. The projected pathlines shown in Figure 2B correspond to the secondary gas motion induced on the X–Y plane. In three dimensions, this motion is superimposed on the rotation around the X-axis, and its strength varies with time. The fluid in the vicinity of the Y axis is thrown outward by the centrifugal forces, while near the stationary container walls, it is dragged to rest. As a result, a clockwise secondary motion is developed on the X–Y plane (see Figure 2B). The predictions of the current model agreed very well with the data reported in Briley and Walls at all instances. Table 1 compares the instantaneous values of the azimuthal velocity at two randomly selected locations of the flow field at $\tau = 0.66$. The excellent agreement shown in Table 1 is typical of all points in the flow domain and was maintained throughout the simulation.

It is well established that cylindrical flows during spinup remain laminar and axisymmetric over a wider range of Reynolds numbers, when compared to their spindown counterparts, which are inherently unstable and become turbulent at relatively low Reynolds numbers. To this end, additional tests were conducted to examine the capability of the current model to provide reliable data under spindown conditions and at even higher Reynolds numbers than those considered herein. Several simulations were performed using different Reynolds numbers in an all-gas rotating-tube flow configuration. Very good agreement between the model predictions and the data of Briley and Walls (1970) was found (Xin 1995) for Reynolds numbers up to 1000.

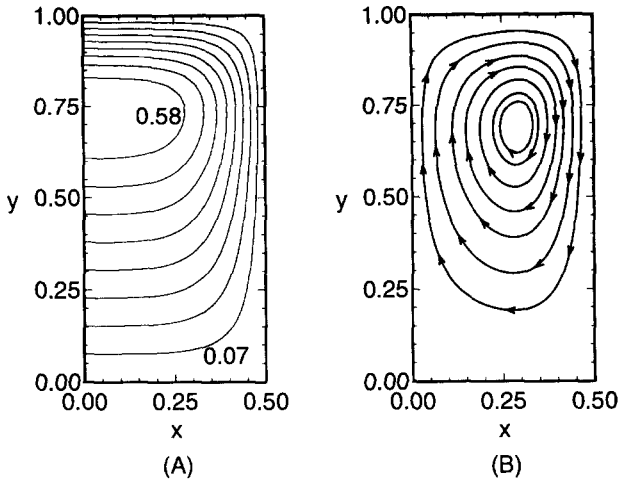

Figure 2 (A) Isocontours of azimuthal velocity component, and (B) projected pathlines calculated using the instantaneous velocity field at $\tau = 0.66$

As a last test, the present model was employed to simulate the ambient flow induced by a rotating sphere suddenly immersed in a quiescent gas. This configuration is of intrinsic interest in the fields of meteorology and astrophysics and has received attention theoretically, experimentally, and numerically. The torque required to keep the sphere rotating at a constant angular velocity was used for comparisons of the current model predictions with the results of Sawatzki (1970), Takagi (1977), and Dennis et al. (1980, 1981). The dimensionless torque M at steady state for various values of the Reynolds number is given in Table 2. As seen in that table, the calculated asymptotic values of M show excellent agreement with previously published results over a wide range of Reynolds numbers.

Multiphase flow simulations

In the base case two-phase flow simulation (Figure 1), the gaseous volume initial motion was specified to be a rigid-body rotation around the X-axis with a constant frequency of 100 Hz (within the high frequency range of practical turbulent flows). The outer vortex radius was $R_0 = 200$ μm, and the gas temperature was assumed to be uniform and equal to 1000 K. The ambient pressure was 1 atm. At $\tau = 0$, a linear array of identical quiescent droplets were placed at equal distances ($2H = 600$ μm) along the axis of the cylindrical vortex. The droplet radii were 100 μm, resulting in a rotational gas Reynolds number of $Re_g = 0.25$. The initial droplet temperatures were uniform and equal to 280 K. The properties of n-decane were assumed for the liquid, as being representative of spray combustion applications. The thermophysical properties of the gas phase were those of air at 600 K and 1 atm. The complete set of geometric parameters

Table 1 Comparison of azimuthal velocities at selected locations at $\tau = 0.66$

Location	Briley and Walls (1970)	Present model
$X/H = 0.56$, $Y/R_0 = 0.73$	0.58	0.579
$X/H = 0.37$, $Y/R_0 = 0.91$	0.364	0.364

Table 2 Dimensionless torque M at steady-state gas rotation versus Reynolds number

Re	Takagi (1977)	Deniss et al. (1980)	Dennis et al. (1981)	Sawatzki (1970)	Present study
1	50.3	50.3	50.3		50.7
50		1.55	1.55	1.55	1.55
100		0.966	0.966	0.966	0.954
500			0.348	0.35	0.367
2000			0.158	0.16	0.15

and thermophysical properties of the two fluids are given in Table 3. The simulation was ceased at $\tau = 24$, when the droplet temperatures became high enough to render the nonevaporation assumption invalid. At that instant, the initially quiescent droplets had assumed a nearly rigid-body rotation with a frequency of ~ 35 Hz. It is noted that although evaporation is neglected, the simultaneous consideration of heat and momentum transport provides useful insight for similar cases involving phase change.

Figure 3 shows the influence of each droplet on its immediate vicinity in terms of the isocontours of the azimuthal velocity v_φ. Because the gaseous flow is a solid-body rotation before the introduction of the droplet array ($\tau = 0$), the contour lines of the azimuthal velocity are initially parallel to the sidewall ($y = R_0/r_0$). After the introduction of the droplets, the azimuthal gas velocity component near the droplet surface is suddenly reduced by shear interaction with the quiescent liquid (Figure 3A). As time proceeds, the droplet surface is gradually pulled into motion, as gaseous momentum is continuously transferred into the liquid phase. As seen in Figure 3, the liquid azimuthal velocity component decreases monotonically from the equator to the pole. It is important to emphasize that during that period, the sidewall continues to rotate with constant angular velocity, thus continuously pumping azimuthal momentum into the system. As a result, the azimuthal velocity of both phases near the gas/liquid interface increases gradually, and the contour lines become increasingly flatter (compare Figures 3A and B). Comparing with the gas phase, the momentum diffusion within the liquid is much faster because of its higher viscosity; at $\tau = 24$ the azimuthal velocity contours within the droplet are almost parallel to the sidewall. This means that rigid-body rotation is being approached within the droplet.

The secondary motion in both phases is shown in Figure 4 in terms of instantaneous particle pathline projections on the X–Y plane at four different instances; $\tau = 0.2$, 1.8, 6, and 24. Because of the introduction of the initially quiescent droplets, the azimuthal velocity of the gas is reduced near the droplet surface, where the initial balance between centrifugal and pressure forces is thus disturbed. The decrease of the centrifugal force induces the gas near the equatorial plane to move toward the axis of rotation (Figure 4A). The induced gas secondary motion decays gradually but maintains its counterclockwise direction. The secondary motion within the droplet is more complex and depends on the dynamic interaction between the azimuthal and polar shear stresses as well as the momentum transfer within the droplet itself. At early stages, the liquid secondary motion induced by the rotating droplet surface is still developing and is relatively weak. The secondary motion direction is dominated by the polar shear stress, which drives the surface liquid from the equator to the pole (Figure 4A). As the azimuthal momentum is continuously transferred from gas to liquid, the strength of the secondary motion within the droplet is enhanced. A secondary motion of the opposite direction develops gradually starting from the pole; Figure 4B shows this transition. As time proceeds, the direction of the liquid secondary motion is gradually reversed, and at later times the momentum transfer within the droplet dominates the opposing surface shear stresses (Figure 4C). As the velocity distribution in the droplet approaches rigid-body rotation, the strength of the induced secondary motion decays and eventually dies out, as indicated in Figure 4D.

Typical trajectories of flow-tracing elements within the droplet revealed a helical internal circulation pattern. The paths lie on the same side of the $X = 0$ symmetry plane and have a complex 3-D character as a result of the superposition of the azimuthal rotation with the secondary motion on the X–Y plane (shown in Figure 4). At early times, the liquid particles follow a spiraling motion away from the equatorial plane, while simultaneously moving closer to the pole of the axis of rotation (Figure 4A). After approaching the pole, the fluid spirals inward from the pole to the droplet center, subsequently turns, and finally winds around the X-axis until it reaches its original position near the droplet surface. At later times, a similar internal circulation pattern is found, however, the circulation direction is opposite (Figure 4C).

Table 3 Geometric parameters and fluid thermophysical properties

r_0, m	0.0001	R_0, m	0.0002
H, m	0.0003	σ, N/m	21.4×10^{-3}
ρ_l, kg/m^3	722	ρ_g, kg/m^3	0.59
μ_l, Ns/m^2	8.41×10^{-4}	μ_g, Ns/m^2	2.98×10^{-5}
$c_{p,l}$, J/kg·K	2200	$c_{p,g}$, J/kg·K	1098
k_l, W/m·K	0.13	k_g, W/m·K	0.058

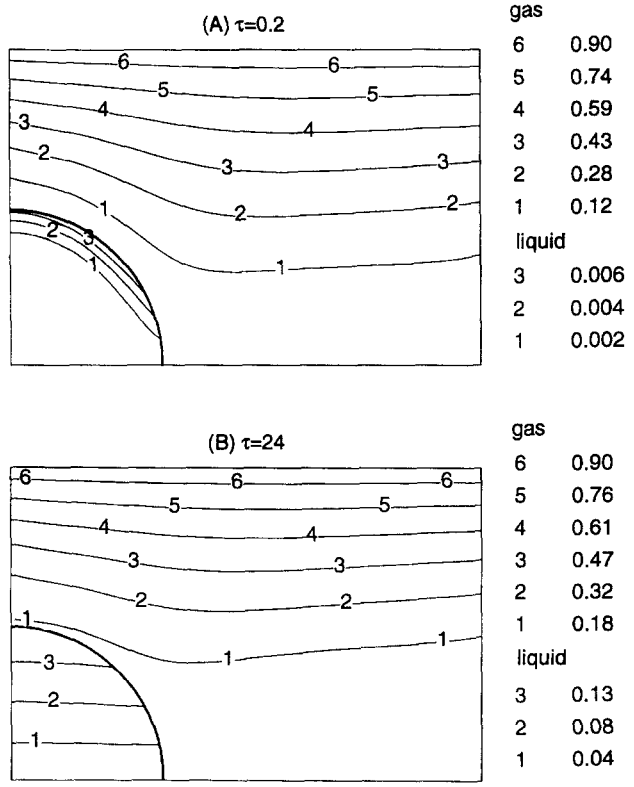

Figure 3 Azimuthal velocity contours in the flow domain at (A) $\tau = 0.2$, (B) $\tau = 24$

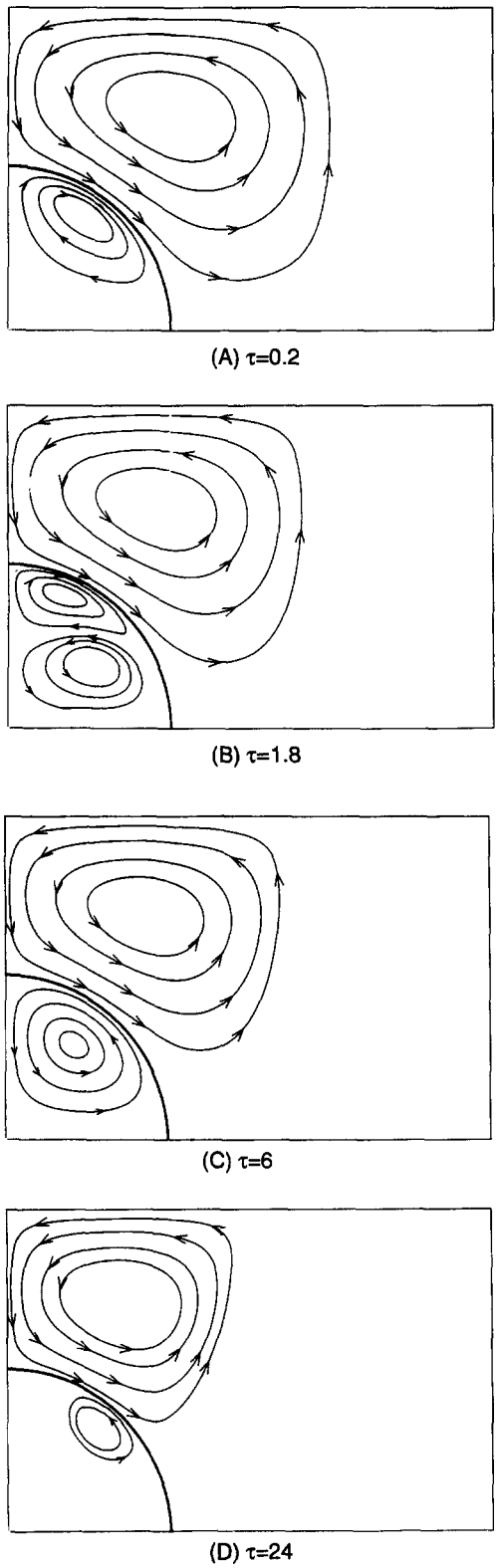

Figure 4 Induced secondary (nonrotational) motion in both phases at four different instances; (A) $\tau = 0.2$, (B) $\tau = 1.8$, (C) $\tau = 6$, and (D) $\tau = 24$

The above trajectories are similar to those reported in Megaridis et al. (1994) and are very different from typical toroidal trajectories within droplets exposed to axisymmetric streams (Hill 1894). It is worth noting, however, that in the present investigation both phases are solved in a fully coupled fashion (including heat transfer); whereas, the helical internal circulation reported in Megaridis et al. was induced by spatially nonuniform droplet-surface rotation.

The dynamic evolution of the secondary motion induced in the liquid phase can be seen in Figure 5A, which shows the transient variation of the polar velocity distribution on the droplet interface ($v_{\theta,s}$). Early on, the negative values of $v_{\theta,s}$ indicate that fluid elements on the droplet surface move from the equator to the pole. As the droplet spins up, the direction of $v_{\theta,s}$ is reversed, its magnitude increases and eventually reaches a peak ($\tau = 12$). As the spinup process slows down, the rigid-body velocity distribution within the droplet is approached, and the polar velocity decays gradually. The normalized values of $v_{\theta,s}$ in Figure 5A show that the induced secondary motion within the droplet is very weak; i.e., $v_{\theta,s} \sim O(10^{-4})$. Based on the calculated values of v_θ in the liquid phase, the typical time period of a closed fluid-element trajectory was found to be of the order of 10 seconds. Using an estimate (Lefebvre 1989) of the time required for complete evaporation, the lifetime of a 100 μm-radius n-decane droplet in quiescent air at 1 atm and 1000 K is about 0.43 s

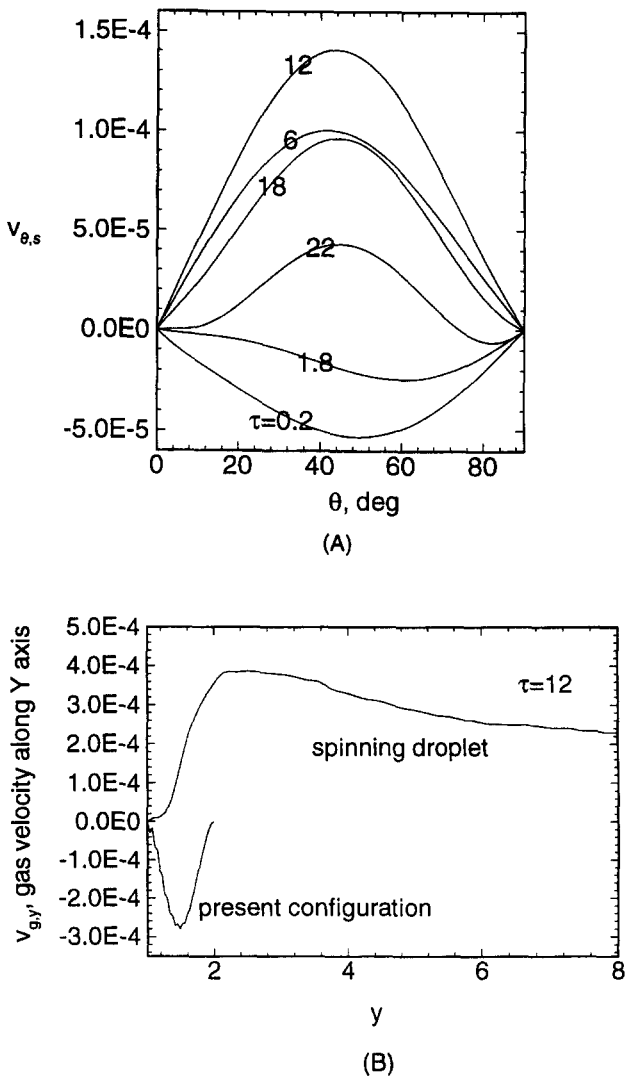

Figure 5 (A) Transient variation of polar velocity profile on the droplet interface, and (B) comparison of secondary gas-phase motion for the rotating flow studied in this paper (Figure 1) and a spinning droplet decelerating freely in quiescent gas

($\tau = 550$). Thus, under conditions that are characteristic of spray combustion applications, the time period of the secondary motion is much longer than the droplet evaporation lifetime. In that respect, the effect of the induced secondary motion within O(100 μm) droplets is expected to be negligible. However, the time period of the secondary motion in the interior of larger droplets can be shorter than the corresponding droplet evaporation lifetime. For example, a similar calculation involving a rotating 1 mm-radius n-decane droplet provided a period of the secondary motion of 4.4 s, which is substantially lower than the estimated (Lefebvre) droplet evaporation lifetime of 43 s.

To assess the strength of the induced secondary motion in the gas phase under the rotational conditions considered in this paper, Figure 5B presents the y-velocity component along the y-axis at $\theta = 90°$ and $\tau = 12$ when the most vigorous secondary motion occurs in the liquid (Figure 5A). The additional (top) velocity profile plotted in Figure 5B corresponds to an initially spinning 100 μm-radius droplet that is suddenly ($\tau = 0$) immersed into a quiescent ambient. The rotation frequency of this spinning droplet (30 Hz around the X-axis) was selected to be similar to the steady-state rotation frequency assumed by the droplets in the array configuration of Figure 1 ($\sim$ 35 Hz). The spinning droplet decelerates gradually because of shear and induces a secondary (nonrotational) motion in the surrounding medium. At $\tau = 12$, the secondary motion caused by the spinning droplet attains a spatial maximum at approximately one droplet diameter from the gas/liquid interface (located at $y = 1$). The comparison of Figure 5B demonstrates that the secondary motion induced in the gas by the spinning droplet is stronger than that encountered when the rotating gas drives the droplet spinup.

In the flow configuration studied herein, shear interaction between the two phases occurs along two directions: azimuthal (φ) as a result of rotation, and polar (θ) as a result of the induced secondary motion. Figure 6 shows the temporal variation of the corresponding shear stresses on the droplet surface. The magnitude of the azimuthal shear stress $\tau_{r,\phi}$ decreases monotonically with time (Figure 6A) as the liquid is induced to rotate. The much weaker polar shear stress $\tau_{r,\theta}$ starts from zero (initially there does not exist secondary motion in gas phase), reaches a maximum at $\tau = 0.2$, and then decreases with time as the rigid-body rotation in the gas phase is attained.

Figure 7 shows the transient behavior of the azimuthal velocity profiles *versus* radial distance from the droplet center along the Y-axis ($\theta = 90°$). Naturally, the azimuthal velocity component on the droplet surface ($y = 1$) increases gradually because of the momentum influx from the gas phase. Because liquid viscosity is much larger than its gas-phase counterpart (Table 3), the momentum transfer within the liquid is very fast. As a result, the azimuthal velocity varies almost linearly with y, thus resembling an accelerating rigid-body rotation. On the other hand, the azimuthal velocity in the gas phase ($1 < y < 2$) is clearly not linear with respect to the radial direction. The accelerating character of this velocity component is caused by the continuing influx of momentum through the vortex sidewall ($y = 2$).

The polar profiles of rotation frequency and azimuthal velocity component on the gas/liquid interface are illustrated in Figure 8 for four different instances of the simulation. From this figure, the gradual enhancement of the azimuthal velocity component on the droplet surface is apparent. As physically expected, this component increases monotonically from the pole ($\theta = 0°$) to the equator ($\theta = 90°$). The local rotation frequency on the droplet surface is also depicted in Figure 8 and shows that within a short time period ($\tau = 0$ to 24), the droplet is accelerated from 0 to 35 Hz. This transient period is appreciably lower than the estimated (Lefebvre 1989) droplet evaporation lifetime ($\tau \sim 550$) under quiescent conditions. This trend clearly suggests that this droplet can be induced to rotate within a small fraction of its evaporation lifetime. It is noted, however, that while the outer gas boundary

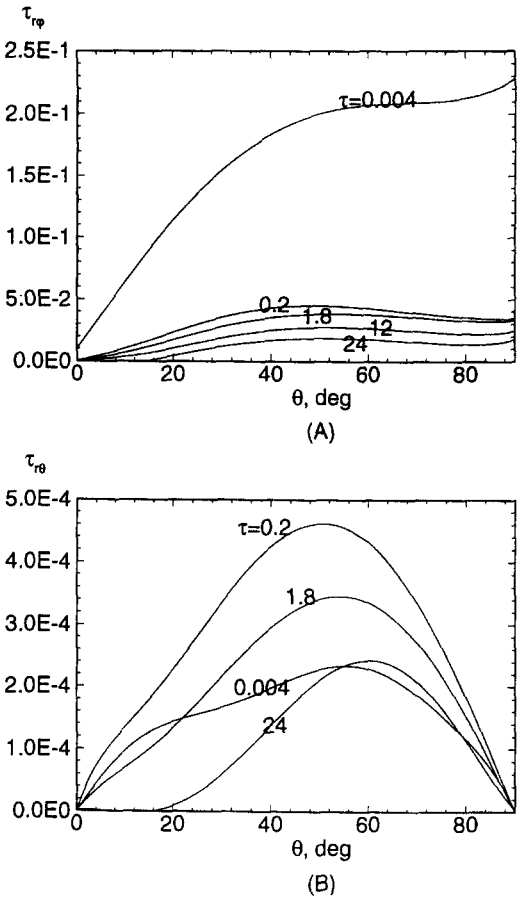

Figure 6 Transient shear stress variation on the droplet interface; (A) azimuthal component, (B) polar component

rotates at 100 Hz, the droplet rotation frequency remains considerably lower (below 40 Hz).

Figure 9 shows the temperature distributions in both phases at two early instances of the simulation. It can be seen that the gas phase is readily cooled by the droplet and that steep temperature gradients are established below the liquid interface. In both fields displayed in Figure 9, the temperature in the droplet core is much lower than that of the interface. Furthermore, the isotherms in the droplet interior as well as in the vicinity of the droplet clearly indicate the dominance of conduction in heat transport along the radial direction under these conditions. The dominance of con-

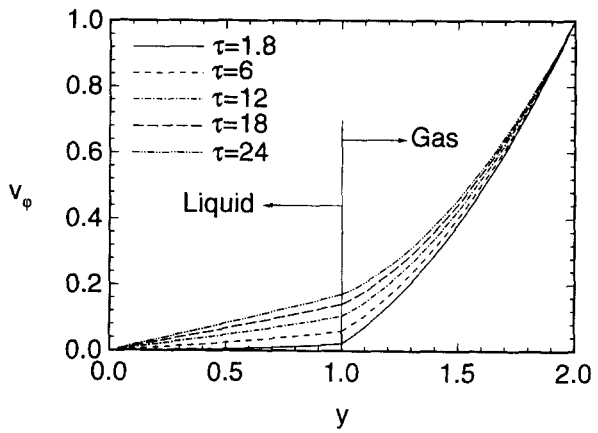

Figure 7 Transient liquid and gas azimuthal velocity variations along the y-axis

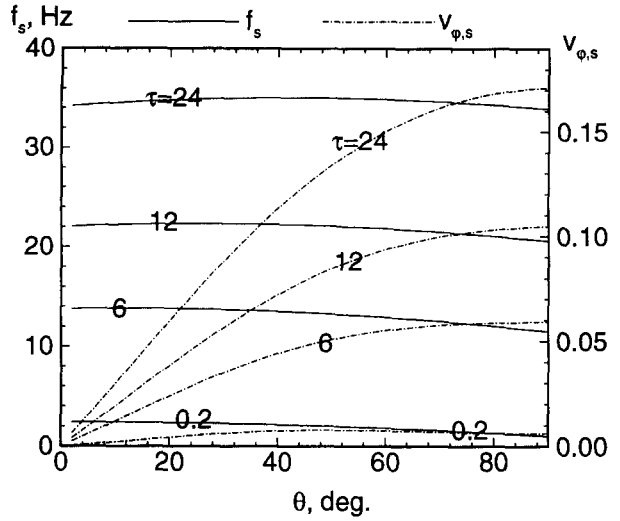

Figure 8 Angular profiles of rotation frequency and azimuthal velocity on the droplet surface

duction was also verified at later times. This calculation also showed that transient droplet heating persists for the entire spinup process. Evaporation, when present, is expected to drain a portion of the energy influx from the gas phase, thus causing a modification of the liquid heating rate. Figure 10 shows the temperature profiles in both gas and liquid phases along the y-axis at $\theta = 90°$. The droplet is heated up gradually, and the temperature nonuniformity in the droplet interior is maintained during this period.

To examine the effects of the induced secondary motion on overall heat transfer rates in the droplet interior, an additional simulation with the same parameters but in quiescent conditions (no rotation) was conducted. The resulting temperature distributions along y at $\theta = 90°$ for this simulation were found to be

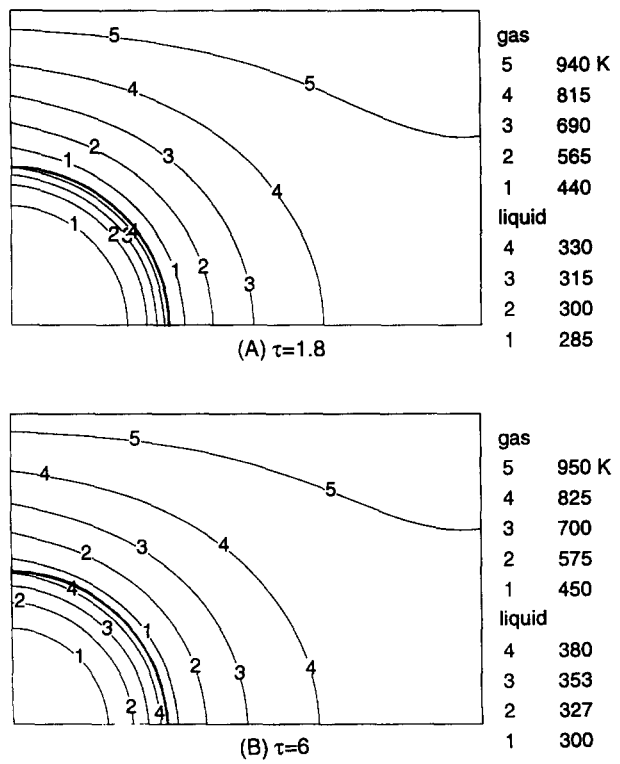

Figure 9 Temperature distributions in both phases at different instances; (A) $\tau = 1.8$, (B) $\tau = 6$

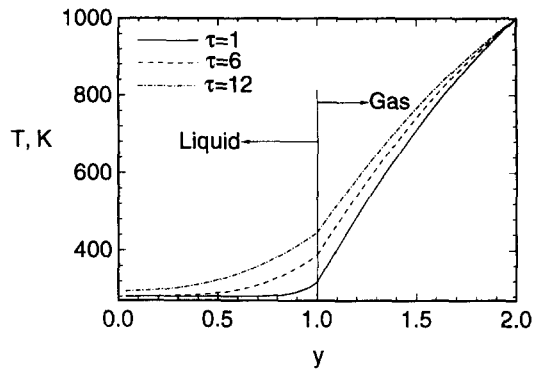

Figure 10 Transient temperature profiles along the y-axis; $y = 1$ corresponds to the droplet/gas interface

nearly identical to those corresponding to the rotating conditions with $Re_g = 0.25$ (see $r_0 = 100$ μm curve in Figure 11). This is an outcome of the extremely weak secondary motion when compared to the rotation around the X-axis (see discussion relevant to Figure 5A). This result also verifies the dominance of conductive heat transfer along the radial direction under the rotating conditions investigated herein. One more simulation was performed involving the same configuration, but a 1 mm-radius droplet trapped in a tubular vortex of 2 mm-radius ($Re_g = 25$). Both rotating and nonrotating conditions were examined for the larger droplet. Figure 11 compares the radial temperature distributions along y at $\theta = 90°$ for rotating and nonrotating conditions. This comparison suggests that heat transfer in the gas phase around larger droplets is enhanced by the induced secondary motion. The increased influence of larger Reynolds numbers on heat transport, under the conditions investigated herein, is anticipated when we examine the form of Equations 6 and 13. It is also of interest that for the higher Reynolds numbers [O(100–1000)] of the experiments of Pearlman and Sohrab (1991, 1993), the enhancing effects of rotation on the evaporation and combustion rates are consistent with the results found herein.

The imposed rotation conditions at the outer wall of the tubular eddy ($Y = R_0$; Figure 1) were considered to be uniform so far. In practice, however, this situation is less likely to occur than others where the rotation frequency at $Y = R_0$ varies with X. To this end, two additional cases were considered to examine the effects of nonuniform azimuthal velocity profiles along x. Linear $v_\varphi(x)$ profiles on the sidewall were employed for simplicity; the rotation frequency varied from 150 Hz at $x = 0$ to 50 Hz at $x = H/r_0$ for Case 2, and from 50 Hz to 150 Hz for Case 3. The geometric parameters in both cases were identical to the base

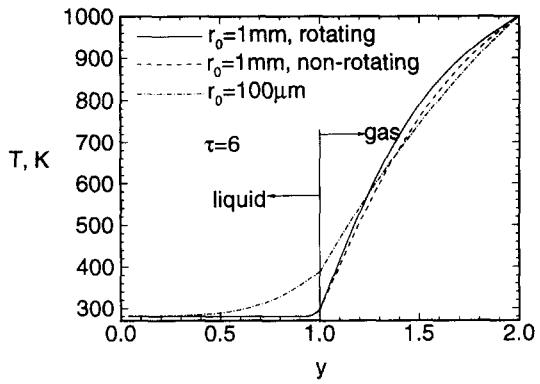

Figure 11 Temperature distributions in both phases along the y-axis at $\tau = 6$; two different sizes are considered under both rotating and nonrotating conditions

case simulation; $r_0 = 100$ μm, $R_0 = 200$ μm, $H = 300$ μm. The gas phase was initially quiescent and had the same temperature (280 K) with the liquid phase. At $\tau = 0$, the outer cylinder surface was induced to rotate in both cases. At the same instant, the temperature of this boundary was changed to 1000 K, thus causing gradual heatup of the system. Figure 12 shows the induced secondary motion in both phases of Cases 2 and 3 at the same instant ($\tau = 10$) of the two simulations. The secondary motion directions in the gas phase are opposite, while the liquid-phase circulation is rather similar. In Case 2 (Figure 12A), the azimuthal velocity on the sidewall is highest at $x = 0$. When the cylinder surface starts to rotate, fluid elements are pushed outward by centrifugal forces. A typical gaseous element moves outward from the vicinity of the droplet equator to the sidewall, then parallel to it, inward toward the axis of rotation, and finally to the droplet pole. Obviously, in Case 3, a typical fluid element follows an opposite path because of the relatively higher azimuthal velocities at $x = H/r_0$. It is worth noting that the direction of the secondary motion in the droplet interior at $\tau = 10$ is the same for both cases, which means that the nonuniformity of azimuthal velocity profiles in the gas phase has little effect on the direction of the induced secondary motion in the droplet interior. This attests to the dominance of centrifugal forces in mass transport within the droplet. As in the uniform-rotation calculation (Case 1), the induced droplet internal circulation in Cases 2 and 3 changes dynamically, and depends on the integrated effects of azimuthal and polar stresses on the interface, as well as the momentum transfer within the droplet. Because of the spatially varying rotation along the cylinder sidewall in Cases 2 and 3, the induced gaseous secondary motion always exists, unlike Case 1 in which the secondary motion eventually decays (see Figure 5A). Although the secondary motion in the gas phase of Cases 2 and 3 was more vigorous than Case 1, the nonrotational velocities within the liquid remained very weak compared to their azimuthal counterparts. As a result, the heat transfer along r was again found to be conduction-dominated.

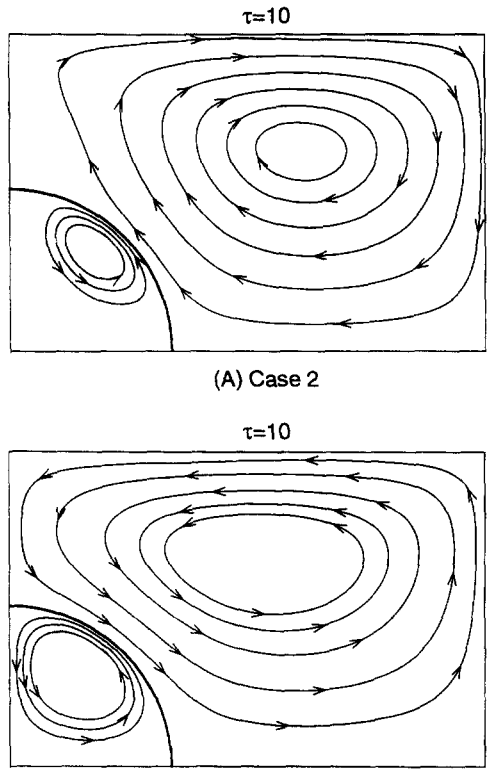

Figure 12 Induced secondary motion in both phases at $\tau = 10$; (A) Case 2, (B) Case 3

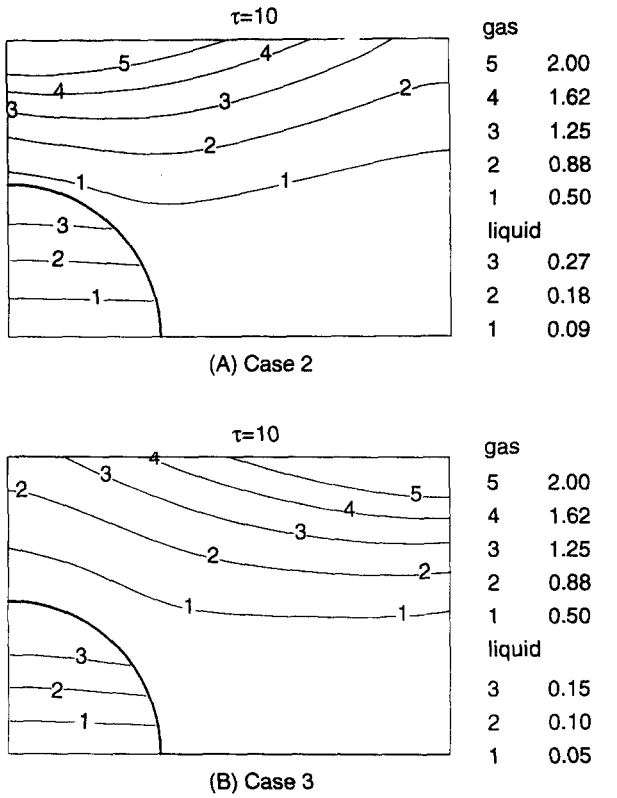

Figure 13 Azimuthal velocity distributions in both phases at $\tau = 10$; (A) Case 2, (B) Case 3

The azimuthal velocity isocontours in both phases of Cases 2 and 3 at $\tau = 10$ are shown in Figure 13. Although the rotational velocities differ considerably along the sidewalls, the azimuthal velocity contour shapes within the droplets are similar. It is noted, however, that the actual values of these velocity components are quite different, reflecting the different sidewall rotation frequencies near the droplet for the two cases (150 Hz in Figure 13A *vs.* 50 Hz in Figure 13B). After a short transient period, the velocity distributions within both droplets approach a rigid-body rotation, as shown by the nearly horizontal character of the contours in Figure 13.

To examine the effect of rotation at conditions characteristic of gas turbine combustors, another calculation was performed with a pressure of 10 atm. The geometric, initial, and boundary conditions were identical to those of the base case simulation at 1 atm. Except for gas density, all other thermophysical properties remain fairly constant with pressure. Thus, the gaseous Reynolds number is ten times higher for the 10 atm case (Re = 2.5 *vs.* 0.25 at 1 atm). As discussed previously, higher gaseous Reynolds numbers result in the enhancement of secondary motion in both phases. However, it was found that this enhancement remains weak when the ambient pressure increases from 1 atm to 10 atm. The model predictions at 10 atm again showed that the induced secondary motion at higher pressures is weak, and the heat transfer along the radial coordinate is conduction-dominated.

Discussion

So far, the effects of rotation on heat transfer and fluid dynamics in both phases have been studied. Our simulations for the axisymmetric configuration seen in Figure 1 showed that the heat flux is little influenced by rotation for droplet sizes relevant to

spray combustion (100 μm-radius or smaller) and vortex rotation frequencies below 100 Hz. Because gasification is dependent — among other factors — upon heat transport, droplet evaporation may be unaffected under the rotation conditions examined in this paper. However, in the absence of evaporation modeling, no firm conclusions can be made, especially for other configurations involving both droplet rotation and translation with respect to the ambient gas.

The model predictions also showed that as the rotational Reynolds number increases (larger droplets or stronger rotation frequencies), the secondary motion becomes increasingly more important, thus affecting the heat flux. As a result, liquid evaporation may be enhanced significantly as the rotational Reynolds number increases. To this end, although a quantitative comparison is not possible, the information obtained from the numerical calculations presented herein is consistent with Pearlman and Sohrab's (1991, 1993) experimental results on droplets that are substantially larger than those encountered in spray combustion applications.

Finally, it is noted that the predicted droplet heating time is shorter than the actual one, because evaporation was not modeled in this study. Evaporation, when present, drains a portion of the energy influx from the gas phase, which results in slower heatup of the liquid phase.

Conclusions

The transient fluid-dynamical and heat interactions between a linear periodic array of nonevaporating droplets and a concentric hot-gas cylindrical volume have been studied in a rotating tube configuration where the gaseous medium drives the initially quiescent droplets into rotation (spin-up). The model considers situations where the angular velocities remain coincident with the tubular axis, thus allowing an axisymmetric formulation for the investigation of gas/droplet interactions within turbulent eddies. The results showed that initially quiescent droplets can be rotationally accelerated within relatively short time periods compared with their estimated evaporation lifetimes. As a result, volatile liquids are expected to vaporize at much lower relative angular velocities (with respect to the surrounding gas) than those encountered at injection. Steady rotation conditions of the outer gaseous boundary induced droplet internal velocities that quickly attained a rigid-body rotation pattern. Even in cases where the steady-state gas-phase motion was not a rigid-body rotation, the droplets were eventually induced to rotate in a rigid-body fashion. The characteristic time periods of transient droplet heating and spin-up were found to be of comparable magnitude. Under the flow conditions considered in this study, the secondary (nonrotational) circulation induced within each droplet remained weak, and the dominant mechanism of heat transfer along the droplet radius was heat conduction. In general, for the flow configuration considered herein and the droplet size and frequency range relevant to practical spray combustors (small rotational Reynolds numbers), the induced secondary motion had little overall influence on heat transport rates. However, this influence was found to be non-negligible for increased Reynolds numbers. Finally, spatially nonuniform rotation modes of the ambient gas were found to have little effect on the direction of the secondary droplet internal circulation, thus attesting to the dominance of centrifugal forces in momentum transport in the droplet interior.

Acknowledgments

Useful discussions with Drs. Joseph Hodges and Cary Presser of NIST are acknowledged with appreciation. The support of the Pittsburgh Supercomputing Center through an allocation of computer time on the Cray C-90 is also acknowledged.

References

Briley, W. R., and Walls, H. A. 1970. A numerical study of time-dependent rotating flow in a cylindrical container at low and moderate Reynolds numbers. In *Proc. 2nd International Conference on Numerical Methods in Fluid Dynamics*, Springer-Verlag, New York, 377–384

Brown, R. A. and Scriven, L. E. 1980. The shape and stability of rotating liquid drops. *Proc. R. Soc. London*, **A371**, 331–357

Chandrasekhar, S. 1965. The stability of a rotating liquid drop. *Proc. R. Soc. London*, **A286**, 1–26

Dennis, S. C. R., Singh, S. N. and Ingham, D. B. 1980. The steady flow due to a rotating sphere at low and moderate Reynolds number. *J. Fluid Mech.*, **101**, 257–279

Dennis, S. C. R., Ingham, D. B. and Singh, S. N. 1981. The steady flow of a viscous fluid due to a rotating sphere. *Quart. J. Mech. Appl. Math.*, **34**, 361–381

Dukowicz, J. K. 1980. A particle-fluid numerical model for liquid sprays. *J. Comp. Physics*, **35**, 229–253

Dwyer, H. A. 1989. Calculations of droplet dynamics in high temperature environments. *Prog. Energy Combust. Sci.*, **15**, 131–158

Faeth, G. M. 1983. Evaporation and combustion of sprays. *Prog. Energy Combust. Sci.* **9**, 1–76

Godsave, G. A. E. 1953. Studies of the combustion of drops in a fuel spray — The burning of single drops of fuel. *Proc. 4th Int. Symposium on Combustion*, 818–830

Hill, M. J. M. 1894. On a spherical vortex. *Phil. Trans. Roy. Soc.*, **185**, 213–245

Hou, S. S. and Lin, T. H. 1993. A liquid-pool simulation of droplet combustion in a swirl flow. *J. Energy Resources Technol.*, **115**, 175–182

Kim, I., Elghobashi, S. and Sirignano, W. A. 1993. Three-dimensional flow over two spheres placed side by side. *J. Fluid Mech.*, **246**, 465–488

Law, C. K. 1982. Recent advances in droplet vaporization and combustion. *Prog. Energy Combust. Sci*, **8**, 171–201

Lefebvre, A. H. 1989. *Atomization and Sprays*. Hemisphere, Bristol, PA, 330–332

Lozinski, D. and Matalon, M. 1992. Vaporization of a spinning fuel droplet. *Proc. 24th Int. Symposium on Combustion*, 1483–1491

Megaridis, C. M., Hodges, J.T., Xin, J., Day, J. and Presser, C. 1994. Internal droplet circulation induced by surface-driven rotation. *Int. J. Heat Fluid Flow*, **15**, 364–377

Pearlman, H. G. and Sohrab, S. H. 1991. The role of droplet rotation in turbulent spray combustion modeling. *Comb. Sci. Technol.*, **76**, 321–334

Pearlman, H. G. and Sohrab, S. H. 1993. Effects of rotation on cellular premixed flames stabilized on rotating porous spheres. *Comb. Flame*, **92**, 469–474

Plateau, J. A. F. 1863. Experimental and theoretical researches on the figures of a equilibrium of a liquid mass withdrawn from the action of gravity. *Annual Report of the Board of Regents of the Smithsonian Institution*, Washington, DC, 270–285

Sawatzki, O. 1970. Das Strömungsfeld um eine rotierende Kugel. *Acta Mech.*, **9**, 159–214

Sirignano, W. A. 1983. Fuel droplet vaporization and spray combustion theory. *Prog. Energy Combust. Sci.*, **9**, 291–332

Sirignano, W. A. 1993. Fluid dynamics of sprays — 1992 Freeman Scholar Lecture. *J. Fluids Eng.*, **115**, 345–378

Spalding, D. B. 1953. The combustion of liquid fuels. *Proc. 4th Int. Symposium on Combustion*, 847–864

Takagi, H. (1977). The laminar incompressible boundary layer on a rotating sphere. *J. Phys. Soc. Japan*, **42**, 319

Tennekes, H. and Lumley, J. L. 1972. *A First Course in Turbulence*. MIT Press, Cambridge, MA, 2–3

Thompson, J. F. 1980. Numerical solution of flow problems using body fitted coordinate systems. In *Computational Fluid Dynamics*, Vol. 1, W. Kollmann (ed.), Hemisphere, Bristol, PA 1–98

Wang, T. G., Trinh, E. H., Croonquist, A. P. and Elleman, D. D. 1986. Shapes of rotating free drops: Spacelab experimental results. *Phys. Rev. Letters*, **56**, 452–455

Xin, J. 1995. Numerical simulations on sprays: Rotation effects and droplet interactions. Ph.D. thesis, University of Illinois at Chicago, Chicago, IL